

# Characterization of Welding Fume from SMAW Electrodes – Part II

*The composition and morphology of SMAW fume particles are determined using advanced characterization techniques*

BY J. W. SOWARDS, A. J. RAMIREZ, D. W. DICKINSON, AND J. C. LIPPOLD

## ABSTRACT

In Part I of this study, an electrical low pressure impactor (ELPI) was used to collect welding fume from E6010, E7018, and E308-16 electrodes and determine number and mass distributions based on fume particle diameter. Fume generation rates were obtained using an improved fume hood design, and bulk fume phases were identified using X-ray diffraction (XRD). Part II of this study makes use of extensive characterization work by evaluating fume particles (collected in different size ranges with the ELPI) with scanning electron microscopy (SEM) and X-ray photoelectron spectroscopy (XPS). Transmission electron microscopy (TEM) was used to characterize fume particles in the ultrafine ( $< 0.3 \mu\text{m}$ ) range. Using these tech-

niques, fume particles were classified into three distinct morphologies: spherical, irregular, and agglomerate. Agglomerates were the most common particle type observed followed by spherical and irregular. Many of the spherical and agglomerated particles exhibited a core-shell structure where a core, rich in metal oxides, was coated with a shell consisting of more volatile elements (Si, Na, Mg). This core-shell morphology was evident in fumes generated by all three of the shielded metal arc welding (SMAW) electrodes. Extensive chemical analysis was conducted on a large number of particles and agglomerates over the entire size range ( $0.03\text{--}10 \mu\text{m}$ ) collected in the ELPI. Fume composition was found to vary as a function of aerodynamic diameter, which was attributed to the different fume formation mechanisms.

size range (geometric mean diameters between  $0.1$  to  $0.25 \mu\text{m}$ ) while particle mass distributions were shifted to larger particle sizes (mass median diameters between  $0.55$  to  $0.75 \mu\text{m}$ ).

After particle collection with the ELPI, extensive characterization was performed to determine the morphology, composition, and structure of the fume particles in each size range. These characterization techniques included scanning electron microscopy (SEM), transmission electron microscopy (TEM), X-ray energy-dispersive spectroscopy (XEDS), and X-ray photoelectron spectroscopy (XPS). Electron microscopy techniques such as SEM and TEM, often combined with XEDS analytical methods, have been widely used to examine individual fume particle morphology and for performing chemical analysis of both individual and bulk compositions (Refs. 3–5). Scanning electron microscopy is best used to characterize particle morphologies and measure compositions of particles greater than  $0.3 \mu\text{m}$  in size as well as measure compositions of the bulk fume collected in fume filters. Transmission electron microscopy is well suited for imaging particles in the ultrafine particle regime and analyzing particles with microprobe XEDS analyses to find chemical compositions. The electron interaction volume within the particles is a large factor in determining which analysis technique, whether it be SEM or TEM, is better suited to a given particle size because the interaction volume of the beam can vary greatly between the two microscopy techniques. Selected area diffraction (SAD) in the TEM is a useful technique for determining the crystalline structure of the particles.

The XPS is a surface-sensitive analysis technique that analyzes the composition of the sample surface to a depth of approximately  $1$  to  $3 \text{ nm}$  (Ref. 6). The basic principle of XPS uses the photoelectric effect where photoelectrons are emitted from a surface illuminated by a source of (X-ray) photons. This XPS is capable of determining valence states of surface atoms on the sample by measuring binding energies of emitted photoelectrons. This

## Introduction

Welding fume produced by the shielded metal arc welding (SMAW) process contains a variety of metallic and nonmetallic elements and compounds that result from the melting and vaporization of the metal core wire and flux coating of the electrode. Part I (Ref. 1) of this investigation determined the fume generation rate (FGR), particle number, and mass distributions as a function of particle size, and bulk fume chemistry generated by the three SMAW electrodes (E6010, E308-16, E7018) included in this study. Particle number and mass distributions (as a function of fume particle aerodynamic diameter) were determined using an electrical low pressure impactor (ELPI) as described in Part I. The ELPI system was designed to collect and measure particle size distributions with aerodynamic diameters

in the range of  $30 \text{ nm}$  to  $10 \mu\text{m}$ , with a response time of less than  $5 \text{ s}$  (Ref. 2). The system charges particles with a corona charger before they are collected in a low-pressure impactor. The impactor separates the particles by aerodynamic diameter, and as the particles impact each separation stage, the charge is recorded with highly sensitive electrometers. This allows real-time determination of particle size distributions. Gravimetric analysis can also be performed on the individual stages to determine particle mass distribution. Particle number distributions measured in Part I (Ref. 1) showed that fume particles generated by the three electrodes were contained largely in the ultrafine particle

## KEYWORDS

Electrical Low Pressure Impactor (ELPI)  
X-Ray Diffraction (XRD)  
Scanning Electron Microscopy (SEM)  
Shielded Metal Arc Welding (SMAW)  
Welding Fume

J. W. SOWARDS (jeffrey.sowards@nist.gov) and D. W. DICKINSON are formerly with, and J. C. LIPPOLD is currently with the Welding & Joining Metallurgy Group, The Ohio State University, Columbus, Ohio. A. J. RAMIREZ is with the Brazilian Synchrotron Light Laboratory, Campinas, SP, Brazil.

**Table 1 — Aerodynamic Cutoff Diameter (Dp) of ELPI Stages**

Stage	1	2	3	4	5	6	7	8	9	10	11	12	13
Aerodynamic Dp (µm)	0.0284	0.056	0.0947	0.158	0.263	0.384	0.616	0.952	1.61	2.40	4.01	6.71	9.95

technique also has the ability to remove surface layers by using Ar<sup>+</sup> ion bombardment (or etching), thus providing depth profiling capabilities. Between each successive Ar<sup>+</sup> etch, composition can be measured and compared with etching time to provide a composition profile of the sample as a function of analysis depth. Applying this XPS depth profiling technique to welding fume has shown varying composition through the volume of fume particles where the surfaces generally consist of more volatile elements and particle centers are generally metals and their oxides (Refs. 3, 7, 8).

Welding fume particles exist across a large size range from several nm up to several µm in diameter as a result of different particle formation mechanisms (Refs. 9–11). The smallest fume particles (< 100 nm) are formed by homogeneous nucleation from metal and flux vapors. The nucleated particles may experience growth by condensation of additional vapors on particle surfaces. Particle growth by condensation occurs until particles reach an upper limit of approximately 300 nm in diameter (Ref. 9). Accumulation, or growth by collision of particles, results in formation of agglomerates and spherical particles larger than 300 nm. Particles formed by any of these modes may have different composition because the formation mechanism is different. However, the agglomerated particles formed by collision of smaller particles have a composition corresponding to the average of the particles that collided.

Fume contains multiple chemical species, all of which have different volatilities. Less volatile species condense on nucleated particles first (Ref. 9). As temperature decreases, this is followed by condensation of species with increasing volatilities, resulting in the formation of shelled particles. These core-shell particles have been observed in a variety of welding fumes that condense from multiple chemical species (Refs. 7, 8, 11–14). Fume particles possessing the core-shell structure can have distinct surface chemistries from the bulk of the particle, which should be considered during particle characterization.

Due to the large distribution of particle sizes and compositional inhomogeneities, it is necessary to examine each size range independently from the others, and utilize different techniques to fully characterize the nature of welding fumes. This is possi-

**Table 2 — Weld Deposit and Base Metal Compositions\***

Element	AISI A36	AISI 304L	E6010**	E7018	E308-16**
C	0.18	0.019	0.15	0.085	0.086
Mn	0.70	1.46	0.56	0.81	0.95
Si	0.19	0.29	0.20	0.19	0.61
P	0.012	0.033	< 0.005	< 0.005	0.019
S	0.020	0.001	0.020	0.014	0.015
Ni	0.10	8.34	0.048	0.11	9.13
Cr	0.064	18.27	0.063	0.15	19.75
Mo	0.022	0.47	0.018	—	0.22
Cu	—	0.34	—	—	0.12
Fe	Bal	Bal	Bal	Bal	Bal

\*Carbon and sulfur analyzed by LECO technique, all others by ICP or ICP/MS technique.

\*\*Represent compositions from the low-heat input conditions.

ble by using SEM-XEDS for larger (accumulated) particles, and TEM-XEDS for smaller (nucleated) particles. X-ray photoelectron spectroscopy is also important for surface characterization because particles often exhibit a surface composition different from the bulk particle, such as an oxide-rich or light element-rich layer (Refs. 4, 7). These techniques were therefore used in the following study to complement particle size distribution and bulk fume chemistry data provided in Part 1.

**Procedure**

The ELPI was used to collect samples for SEM, TEM, and XPS analysis. This system separates particles by cascade impaction and deposits them on Al-foil substrates placed on each ELPI collection stage. Al collection substrate is used because it is highly conductive, making it suitable for use with electron microscopy and XPS. Also, Al was not a major component of any of the fume that was studied. Table 1 shows the average aerodynamic particle diameters collected by each of the 13 collection stages of the ELPI. Transmission electron microscopy samples were collected by briefly passing carbon-coated copper TEM grids through the fume plume at distances of approximately 75 and 150 mm (3 and 6 in.) above the arc during welding. It was determined that the entire particle size distribution range was collected onto the grids using this method. A detailed procedure for collection and analysis developed previously (Ref. 5) was followed for collection and characterization procedures for each of the electrodes. Compositions of the base materials and actual weld deposits for

each electrode are presented in Table 2.

The scanning electron microscopy analyses were performed using conventional and high-resolution scanning electron microscopes JEOL LV-SEM JSM 5900LV and JEOL FEG-SEM JSM 6330F, respectively. X-ray energy-dispersive spectroscopy analyses were performed using a microanalysis system NORAN Voyager attached to the conventional SEM.

The aluminum foils used to collect the fumes in the ELPI were secured to the SEM sample holder using electrically conductive tape. In addition, examination of TEM grids in the SEM was possible with the use of a specially designed graphite sample holder.

The SEM analyses were performed using 10 to 30 kV and a pole piece to sample distance of 5 to 10 mm. The XEDS analyses were performed at 15 keV using a live spectrum collection time of 100 s, providing excellent peak to background ratios. Certified standards were used to calibrate the XEDS system and as a reference for the quantitative analyses.

The quantitative analysis used a digital top hat filter for background subtraction and ZAF matrix correction method, both integrated to the Voyager system. Fume deposited on stage collection substrates in piles directly below impactor jet orifices. Bulk stage composition measurements were obtained on each stage by defocusing the electron beam to cover a large area of the piles. Therefore, a large number of particles were simultaneously generating X-ray signals during XEDS measurements.

Semiquantitative composition analysis of ultrafine particles was performed with the added capability of XEDS to the TEM.

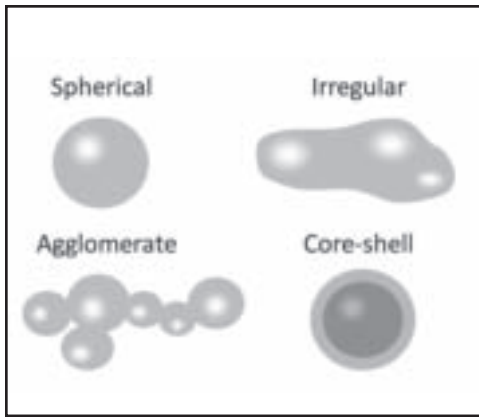


Fig. 1 — Schematic of observed particle morphologies found in SMA welding fume.

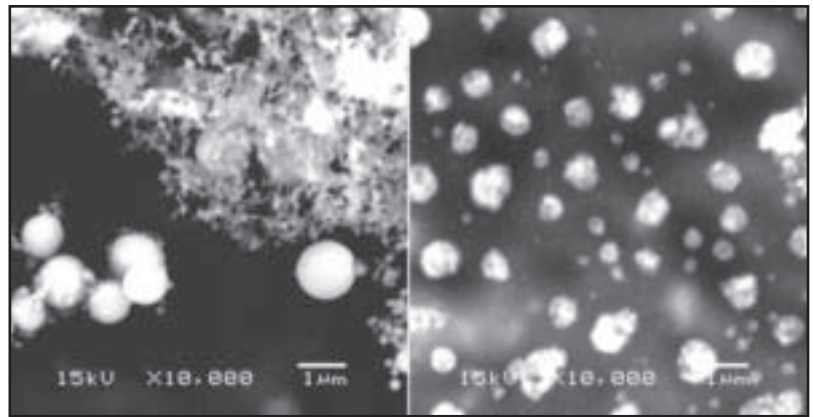


Fig. 2 — An SEM micrograph of fume particles collected with the ELPI. Shown (left) are stage 10 E6010 particles consisting of agglomerates of spherical particles and (right) stage 3 E308-16 showing spherical agglomerates.

The TEM allowed the morphological and chemical characterization of particles of much smaller physical diameters due to the technique's finer spatial resolution. The narrow volume of material exited by the electron beam allowed localized chemical analysis of the ultrafine particles.

Chemical elements with atomic numbers lower than Na and C become difficult to quantify with the XEDS technique for a diffusion vacuum pumped SEM and TEM, respectively. Because of this, oxygen was often eliminated from the quantification routines even though most particles were heavily oxidized. Among the difficulties for oxygen XEDS quantification, the low-energy O-K X-ray photons are highly absorbed by very thin C contamination films. These films are very common in SEMs and TEMs, which severely compromises such element quantification. Al was also left out of the analysis because the Al substrates on which the particles are collected resulted in a large stray signal during XEDS analysis. In addition, fluorine was not quantified in most of these samples due to the F-K X-ray peak overlap with the highly excited Fe-L X-ray peak, making such element quantifi-

cations difficult.

The XPS analysis was performed on particles collected on stage 3 of the ELPI system. The XPS system was a Kratos Ultra Axis XPS and UPS system with depth profiling capabilities using Ar ion etching. Initial survey scans were completed for each sample to determine the elements contained within particle surfaces. Detailed region scans were then performed for each element observed to obtain higher signal-to-background ratios. Samples were then etched with Ar<sup>+</sup> ions for a period of 10 min. Region scans were performed again to observe changes in peak intensity after the etching sequence.

### Results and Discussion

The initial particle characterization was performed with SEM and XEDS analysis because particle morphology and bulk composition of each ELPI stage are most easily obtained with these two techniques, respectively. Magnifications in excess of 100,000 $\times$  were readily obtainable with field emission SEM, allowing for imaging of particles at the larger end of the ultrafine region (di-

ameters < 100 nm). Therefore, this technique was used to image particles from all of the ELPI stages, but worked best on stages 3–13. Three distinct particle morphologies were observed, namely spherical, irregular, and agglomerated. Spherical particles were the most abundant type of individual particle. Irregular particles were generally rod shaped and not as common as the spherical ones. Agglomerates were found to consist of anywhere from several to hundreds of spherical and irregular particles bound together. A schematic representation of the types of particles observed is shown along with a schematic of the core-shell structure, which was observed at high magnifications during TEM analysis — Fig. 1.

### SEM – Particle Morphology

Spherical and agglomerated particles were observed on each stage of the E6010 collections, but individual spherical particles were present in low percentages on the lower stages (1–6). Many of the agglomerates consisted of loosely packed spherical particles with diameters on the

Table 3 — Estimated Volumetric Percentage of Particles from SEM Analysis of the Individual ELPI Stages

ELPI Stage	Spherical Particles		Irregular Particles		Agglomerates	
	E6010	E308-16	E6010	E308-16	E6010	E308-16
1	—	—	~ 70	—	~ 30	—
2	—	—	~ 80	—	~ 20	—
3	—	—	< 2	~ 10	> 98	~ 90
4	—	—	< 2	~ 10–15	> 98	~ 85–90
5	—	—	< 2	~ 10–20	> 98	~ 80–90
6	—	—	< 2	—	> 98	100
7	< 2	—	< 2	—	> 96	100
8	< 6	~ 20–30	< 2	—	> 92	~ 70–80
9	~ 40–50	< 20	—	—	~ 50–60	> 80
10	~ 50–60	~ 50	—	—	~ 40–50	~ 50
11	~ 60–70	< 10	—	—	~ 30–40	> 90
13	—	—	~ 30	—	~ 70	—

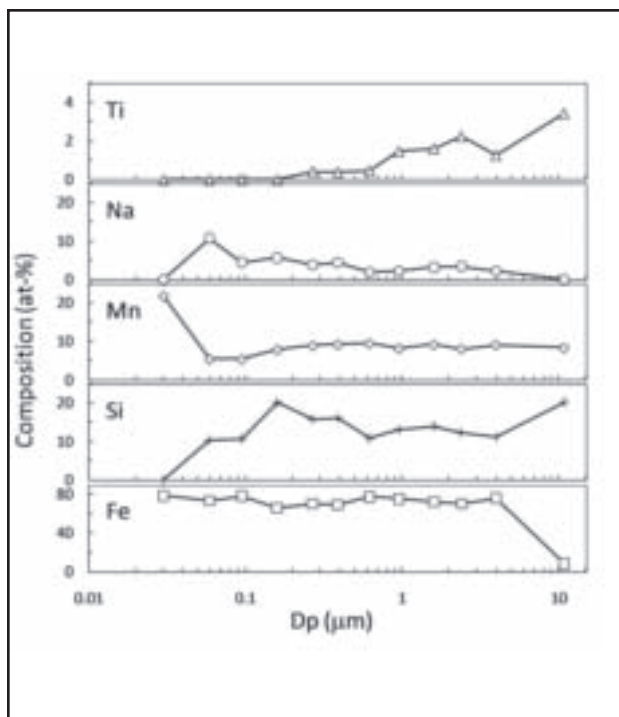


Fig. 3 — Bulk composition of ELPI stages as a function of aerodynamic particle diameter for the E6010 fume. Note different scales of y axes.

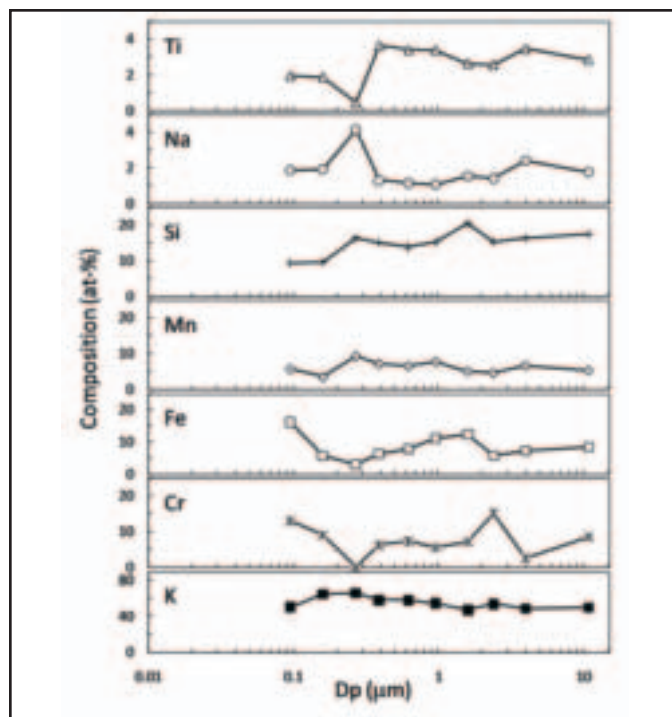


Fig. 4 — Bulk composition of ELPI stages as a function of aerodynamic particle diameter for the E308-16 fume. Note different scales of y axes.

order of tens of nanometers. Irregular particles were observed on all stages as well, but were most prevalent on stages 1 and 2. A qualitative bulk estimate of E6010 and E308-16 particle types was performed with SEM on each of the ELPI stages. This estimate, provided in Table 3, should only be regarded as indicative of the distribution of particle morphologies in each stage.

E308-16 fume morphology distribution was similar to E6010 where the highest percentage of individual spherical particles was observed on the upper stages. A large number of agglomerates were found on all the stages for the E308-16 samples, though they were quite different from the agglomerates found in E6010 fume. These agglomerates were generally well packed together, and in some cases formed large consolidated round agglomerates consisting of multiple fume particles of different sizes. These round agglomerates were most prevalent on stages 3–6. On stages 7–11, there were more loosely packed agglomerates similar to the open-structured type observed in E6010 fume. However, during E308-16 fume morphology analysis, most of the agglomerates were generally observed to be spherical in shape and apparently consolidated. Representative secondary electron micrographs are shown for E6010 and E308-16 fume collections — Fig. 2. E7018 fume particle morphology as a function of size was generally consistent with the observations of

E6010 fume as well, except irregular particles were observed with lower frequency.

To verify the extent of particle agglomeration occurring before collection in the ELPI, carbon-coated TEM grids were passed through the fume plume at different distances during welding. These grids were examined with SEM using a specially designed stage capable of accepting TEM grids. Examination of particles deposited on the grids showed that agglomerates collected from the plume were representative in size of those observed on ELPI stages. Further agglomeration or deagglomeration was determined to be minimal during ELPI collection.

**SEM – Chemical Analysis**

The SEM-XEDS measurements were

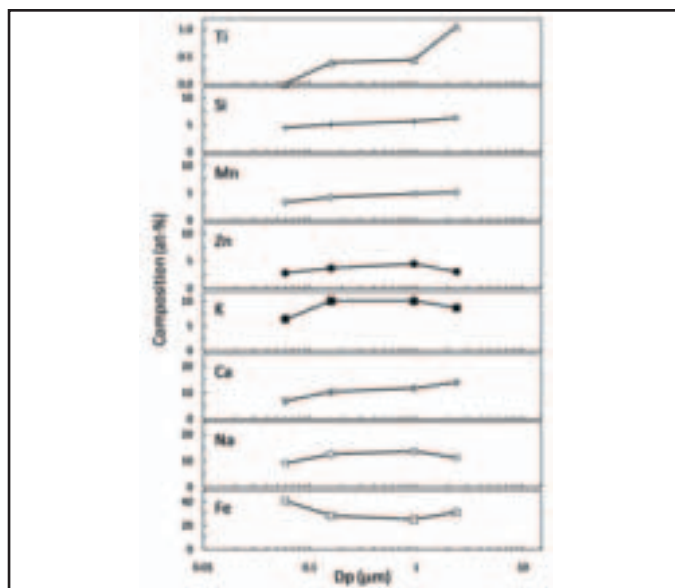


Fig. 5 — Bulk composition of ELPI stages as a function of aerodynamic particle diameter for the E7018 fume. Note different scales of y axes.

performed on stages 1–13 of the ELPI column for E6010, stages 3–13 for E308-16, and stages 2, 4, 8, 10 for E7018 fume collections. These measurements were performed to determine fume composition as a function of aerodynamic diameter, and to analyze individual particles and agglomerates greater than 0.3 micrometers in size. Little fume was present on stages 1 and 2 of the E308-16 collection because size dis-

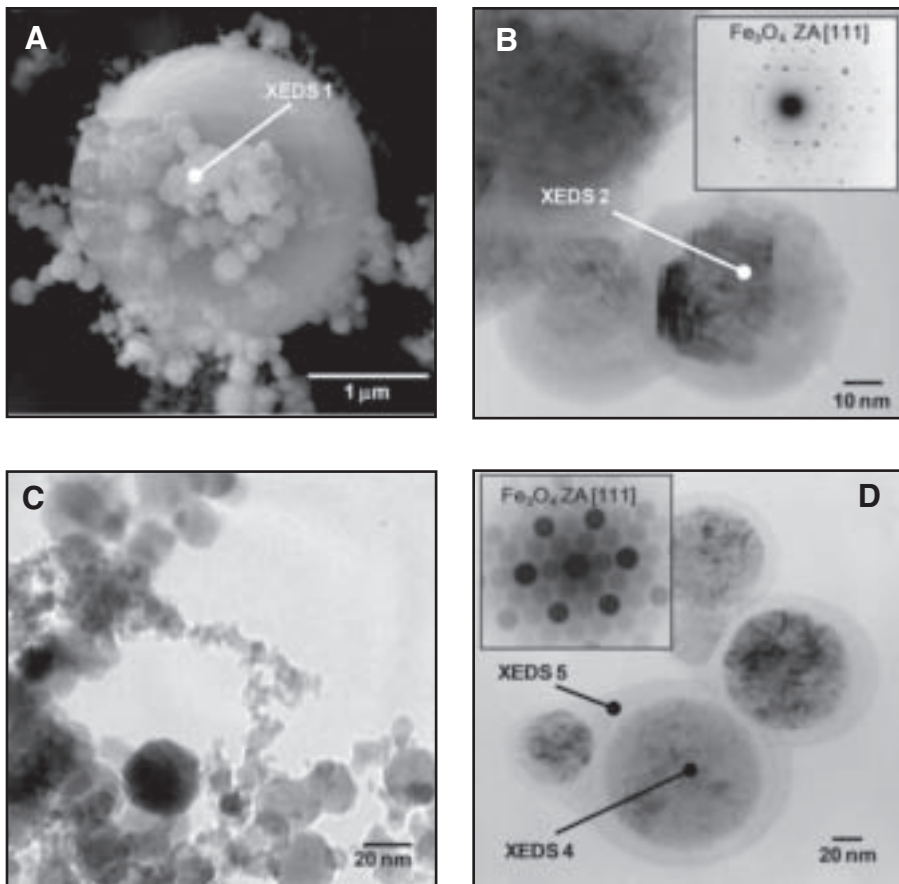


Fig. 6 — Electron micrographs taken with SEM (A) and TEM (B, C, and D). The XEDS measurement locations are indicated on each micrograph except for XEDS 3, which was measured over the entire agglomerate in (C) by spreading the electron beam.

tributions were skewed toward larger diameters. As fume particles were not observed in large piles on those stages, a statistically meaningful measurement of bulk composition of fume deposited on those stages was not possible.

**E6010**

Measured bulk compositions (in at.-%) of E6010 fume collected on ELPI stages are plotted as a function of aerodynamic diameter (Dp) — Fig. 3. Na de-

creases in concentration from 10 at.-% to zero as particle size increases toward the larger diameters. Si is present in rather low concentrations on lower stages but increases to its maximum level just above 0.1 μm. Fe is fairly uniform in composition except in the presence of high amounts of potassium (K) (50.6 at.-%) on stage 13; however, K was not present in detectable levels on the other stages. Ti was also present in low concentrations and observed initially on stage 5 (0.4 at.-%) and peaked in concentration on stage 13 (3.4 at.-%). Both Ti and K are contained in the flux coating of the E6010 electrode. Due to the lack of fluoride present in the E6010 fume, potassium would likely be present as an oxide that would have lower volatility than a potassium-fluoride (KF) compound. This could shift the distribution of K-bearing particles to larger sizes as compounds with lower volatilities preclude vaporization, whereas vapor-condensed particles (such as those containing the more volatile KF compound) would dominate the fume distributions in the smaller particle diameters (Refs. 11, 15). This reasoning may also explain why Ti increases in concentration with increasing particle diameter. Mn was found in highest concentration (21.8 at.-%) in stage 1 (0.03 μm Dp) of the ELPI. It decreased to approximately 8

at.-% in the larger sizes and remained fairly constant as a function of Dp. The enrichment of Mn in the nucleation range of fumes produced during gas metal arc welding (GMAW) with ER70S-3, more specifically in primary spherical particles with diameters < 0.06 μm, has been explained by the degree of supercooling a particle experiences from vapor (Ref. 16). Smaller particles experience larger degrees of supercooling from the initial fume vapor, resulting in higher Mn contents. It is expected that primary particle formation in fumes generated during SMAW would occur in a similar manner. Considering that chemical species from the welding flux condense after the metallic particles nucleate, because they are generally more volatile, the same type of Mn enrichment is anticipated in the smallest SMAW fume particles. This is shown in Fig. 3 where Mn increases in concentration on stage 1.

Approximately 15 individual particles were analyzed with XEDS on each stage. The composition of these particles was generally more complicated than those of the bulk analyses because of the presence of minor additional elements not detected in bulk measurements. Individual analyses were also made difficult because large Al-K and O-K X-ray signals were generated by the background substrate holding the particles. These peaks were subtracted from the X-ray spectra generated

Table 4 — Composition Ranges (at.-%) for Individual Particles and Agglomerates as Measured with SEM-XEDS

Element	E6010		E7018		E308-16	
	Min.	Max	Min.	Max	Min.	Max
Mn	2.8	10.1	1.8	4.4	2.8	7.4
Fe	42.2	77.2	7.7	27.1	3.6	37.7
Si	3.2	17.5	1.8	8.2	1.5	17.9
Na	2.4	12.2	5.3	22.2	0.5	2.6
Ti	0.0	0.6	0.2	2.1	1.1	30.1
Mg	0.3	0.6	0.9	1.9	0.0	0.0
S	0.2	1.0	0.3	0.3	0.4	1.6
Cl	0.2	0.3	0.0	0.0	0.4	5.8
K	2.7	2.7	1.5	4.3	14.1	50.3
Ca	0.0	0.0	0.7	16.8	0.2	22.7
Cr	0.5	0.5	0.0	0.0	3.0	23.4
F	0.0	0.0	7.5	22.1	0.0	0.0
Zn	0.0	0.0	0.5	6.4	0.0	0.0

**Table 5 — Composition of Individual Particles and Agglomerates from the SEM-XEDS and TEM-XEDS Measurements Shown in Fig. 6**

Element	XEDS 1		XEDS 2		XEDS 3		XEDS 4		XEDS 5	
	wt-%	at.-%	wt-%	at.-%	wt-%	at.-%	wt-%	at.-%	wt-%	at.-%
O K*	32.1	50.1	9.7	25.0	—	—	5.3	15.8	16.7	30.3
F K	12.8	16.9	—	—	—	—	—	—	—	—
Na K	5.1	5.6	1.7	3.0	—	—	—	—	—	—
Mg K	—	—	—	—	—	—	0.2	0.4	—	—
Si K	5.6	5.0	8.1	12.0	2.0	3.8	3.9	6.6	51.2	53.0
S K	—	—	0.1	0.2	—	—	—	—	—	—
Cl K	—	—	—	—	—	—	—	—	—	—
K K	3.0	1.9	—	—	1.1	1.6	—	—	—	—
Ca K	11.7	7.3	—	—	—	—	—	—	—	—
Ti K	0.2	0.1	0.1	0.1	—	—	0.2	0.2	—	—
Cr K	—	—	—	—	—	—	—	—	—	—
Mn K	4.1	1.9	8.9	6.7	1.3	1.3	10.0	8.7	1.6	0.9
Fe K	25.5	11.4	71.3	52.9	95.6	93.3	80.3	68.2	30.6	15.9
Zn K	—	—	0.2	0.1	—	—	—	—	—	—

\*Note: O was included in the quantifications to show its presence in these particles, but values are not accurately measured with XEDS.

during the analyses, introducing some error into the measurement. Composition ranges for individual fume particles and agglomerates are provided in Table 4, which shows that some of the particles contained low levels of Cr, K, Ti, Mg, and S in addition to those shown in Fig. 3 (bulk compositions). However, elemental compositions of individual particles were generally in agreement with bulk analyses performed on the same stage.

**E308-16**

Bulk compositions of the E308-16 fume on the ELPI stages showed more scatter than the E6010 fume with respect to the levels of Mn, Fe, and Cr — Fig. 4. These three metals all varied in level and remained below 20 at.-% across the particle size range. Fe, Cr, and Ti had minima in concentration on stage 5 ( $D_p = 0.263 \mu\text{m}$ ) of the ELPI and increased in concentration from stage 5 in both the finer and larger particle diameters. Na decreased in concentration with an increase in particle size, whereas Si increased from approximately 10 to 20 at.-%. Analyses of individual particles and agglomerates shown in Table 4 were in agreement with the bulk analyses, although XEDS spectra of individual particles occasionally revealed lower levels of K and higher levels of Fe. It is also worth noting that K and Cr were simultaneously present in many individual particles, and were measured across the entire collected size range. This observation, along with the X-ray diffraction (XRD) data showing  $\text{K}_2\text{CrO}_4$  in bulk E308-16 fume in Part 1, suggest that the Cr(VI) valence is possible in all particle sizes. However, fur-

ther examination would be necessary to determine the extent of its presence as a function of particle size.

**E7018**

The ELPI stages 2, 4, 8, and 10 were analyzed for the E7018 fume. Bulk compositions are shown as a function of aerodynamic particle diameter — Fig. 5. Mn and Fe are present in lower concentrations than those found on the E6010 stages. This is largely due to the presence of high concentration of the compounds NaF and  $\text{CaF}_2$  in the E7018 fume. Ca appeared to increase in concentration as a function of particle diameter, though the extent of that increase was not large. The F-K X-ray peak overlap with Fe-K prevented accurate measurements of fluorine concentration, and there are obvious problems with oxygen quantification. Therefore, little could be said about the competition of Na and K forming oxide or fluoride compounds, and how this would ultimately affect the distribution of particle size due to different volatilities of those compounds. The E7018 fume generally had high fluorine (based on qualitative comparison of F-K and  $\text{Fe-K}_{\alpha}$  X-ray peak heights) and sodium content in the finer spherical particles, which is expected of elements with higher volatilities. Also, fluorides were present in high concentration in bulk fume according to XRD (Ref. 1). This supports previous explanations (Refs. 9, 11) that fluorides increase the number concentration of finer particle sizes and was shown in particle number distributions of E7018 measured with the ELPI (Ref. 1). Zn measured in the E7018 fume was part of

electrode coating formulation, but virtually none was detected in the weld deposit. The Zn ended up primarily in larger particles and agglomerates ( $> 1 \mu\text{m}$ ) with the levels shown in Table 4. Irregular particles had slightly different compositions, usually consisting of a large percentage of metallic elements, instead of types typically found in the fluxes such as Ca or Na.

Figure 6A represents a typical secondary electron micrograph of a group of agglomerated particles. The corresponding composition data are shown in Table 5 for the spot analysis location indicated as XEDS 1. This agglomerate was imaged on stage 8 of an ELPI collection of E7018 welding fume. Fluorine and oxygen concentrations are included in the quantification to illustrate their presence. The agglomerate is composed mainly of Fe, O, and F along with the presence of two cations typically found in fluoride compounds (Na, Ca). Individual particle analyses showed that E6010 and E7018 fume particles were fairly uniform in composition for both spherical particles and agglomerations, irrespective of size.

**TEM – Particle Analysis**

Fume particles formed by nucleation (primary particles) and growth by vapor condensation vary in composition with size, but as accumulation of these particles occurs from many primary particles, agglomerates become similar to the bulk fume composition (Ref. 16). This is why many of the particles and agglomerates analyzed with SEM do not exhibit much variation in composition with particle diameter. The particle and agglomerate compositions measured with SEM-XEDS

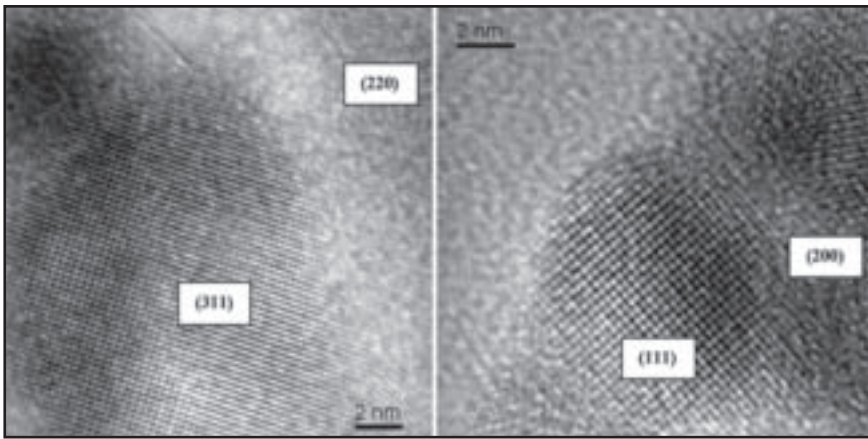


Fig. 7 — High-resolution (HR) TEM micrographs of E7018 ultrafine particles of  $\text{Fe}_3\text{O}_4$  and  $\text{CaF}_2$ .

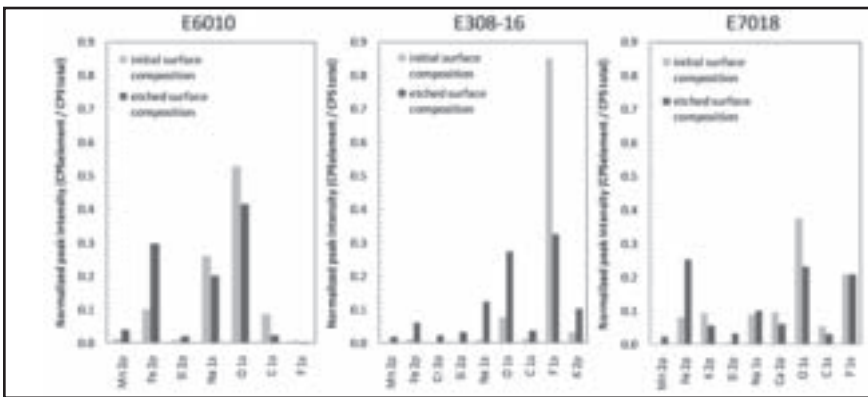


Fig. 8 — The XPS peak intensities as a function of etching for three welding fumes analyzed.

(> 300 nm diameter) were well above the size range where particles forming via a nucleation and growth mechanism are expected to be found. The TEM work was performed on particles less than 300 nm to better capture the composition of particles formed via the nucleation and growth mechanism.

Extensive TEM analyses were performed on fume samples collected from each electrode. A nano-scale agglomerate of several particles generated from E6010 is presented — Fig. 6B. The bottom particle was analyzed with XEDS 2, and the composition is shown in Table 5. Note that this composition, as compared with E6010 fume particles from much larger relative sizes, has higher metal (Fe, Mn, Si) content. Part of a relatively large agglomerate generated during E7018 welding is also shown — Fig. 6C. An average composition (XEDS 3) of this agglomerate was measured by spreading the electron beam to interact with the entire agglomerate. All of the spherical particles within the agglomerate are likely primary particles that are rich in metals (Fe, Mn), the alkali metal K, the metalloid Si, as well as being deficient

of oxygen.

The TEM results showed a core-shell structure was present in fumes from all three electrode types. These particles tend to have an inner core consisting of iron and manganese in the form of a  $\text{Fe}_3\text{O}_4$  type iron oxide (magnetite). Surrounding the core is a coating (or shell) of different composition. An amorphous silicon-rich oxide was identified as the main constituent in the E6010 and E308-16 shells, while the E7018 shells tended to be much thinner and enriched in calcium (and probably fluorine). Composition analyses of an E308-16 core-shell particle are shown, where XEDS4 denotes the particle core composition, and XEDS5 denotes the composition of the shell — Fig. 6D. Note that concentrations of silicon and oxygen increased drastically from 6.6 to 53 at.-% and from 5.3 to 16.7 at.-%, respectively, while relatively large decreases were observed for Mn and Fe in the shell. This core-shell effect was observed in both spherical and agglomerated particles. Many of the E308-16 particles were of a matrix-precipitate type, where small fume particles consisting of metallic oxides

( $\text{Fe}_3\text{O}_4$  type and  $\text{K}_2\text{MO}_4$  type) were imbedded in a Si-rich matrix. These particles likely occur from collisions of primary particles of different compositions followed by chemical segregation of the different phases driven by minimization of Gibbs energy.

The corresponding SAD patterns of the particles in Fig. 6B and D are shown along with the transmission electron micrographs. The E6010 pattern in Fig. 6B was formed by beam diffraction through all of the crystalline particles in the micrograph. Note this pattern exhibits some indication of diffraction rings, indicating many orientations of magnetite occur within the agglomerate. The convergent beam electron diffraction (CBED) pattern in Fig. 6D identifies an  $(\text{M,Fe})_3\text{O}_4$  type structure along the [111] zone axis. In the magnetite matrix, M may be substituted with Cr and/or Mn. Two high-resolution TEM micrographs of different E7018 particles are shown — Fig. 7. The interplanar spacing of the image on the right side, measured to be 3.1 Å, matches the (111)  $\text{CaF}_2$  plane. This agrees with results obtained from the bulk X-ray diffraction (Ref. 1), but more detailed analysis is necessary to fully and unequivocally identify this phase. Many of these particles with high fluoride content were observed with TEM. This further supports the observed shift of the E7018 number distribution to smaller diameters relative to E6010 and E308-16 number distributions.

The SAD patterns showed the  $\text{Fe}_3\text{O}_4$  type crystal structure was most prevalent in particles found in all three types of fume. As a comparison with the electron diffraction data, XRD results (Ref. 1) revealed that the primary phase present in the three fumes analyzed was  $\text{Fe}_3\text{O}_4$ . Slight diffraction peak shifts suggest that Mn (or Cr when present) is probably acting as a substitution for Fe in the magnetite matrix. The XRD showed additional peaks for the E308-16 electrodes as  $\text{K}_2\text{MO}_4$  and NaF, while the E7018 had additional peaks for NaF and  $\text{CaF}_2$  (Ref. 1). However, these phases were not observed with the same frequency as magnetite during SAD analysis of particles.

#### XPS — Particle Analysis

The XPS was used to obtain information about valence states and for partial depth profiling of fume particles. Because XPS has the ability to bombard the sample with  $\text{Ar}^+$  ions to remove surface layers of the fume particles, the system was used to analyze the composition of the particle shell structures and then remove them via etching to analyze core compositions. Stage 3 of ELPI collections was used for fume analysis (aerodynamic diameter of approximately 0.1  $\mu\text{m}$ ) though XPS results

must be interpreted carefully due to the technique's limited spatial resolution (Ref. 3). These XPS results showing the element intensities in the initial and etched conditions are summarized — Fig. 8. Area counts per second (CPS) was used as an estimate of composition. This corresponds to the area under the intensity vs. binding energy curve for each element peak (Mn 2p, Fe 2p, etc.). The values shown are area CPS of each element divided by total area CPS. The XPS suggested the existence of a core-shell structure in the fume of all three electrodes.

The E6010 fume responded to etching with an increase in Fe, Mn, and Si, and a corresponding decrease in Na, O, C, and F. The E7018 fume was rich in Ca, K, Na, and F prior to etching and showed only trace levels of Mn in the outer layers of the fume. Mn, Fe, and Si in the E7018 fume increased in concentration with etching. Fe peak positions of both fumes (E6010 and E7018) correlated with the  $\text{Fe}_3\text{O}_4$  form of iron oxide, thus complementing SAD and XRD data. Iron also appeared to be present in the metallic state after the etching was completed. Manganese was detected in complex oxides in the fume from both electrodes, but the absolute valence states could not be determined due to the inability to isolate Mn compounds within the spectrum generated by the system. The XPS data suggest that Mn is present in the form of a metal oxide of the  $\text{M}_2\text{O}_3$  and  $\text{M}_3\text{O}_4$  type, giving valence states of  $\text{Mn}^{+2}$  or  $\text{Mn}^{+3}$  in both E6010 and E7018 electrodes. Based on XRD and TEM analysis, it is most likely that Mn is present as a substitutional element in the  $\text{Fe}_3\text{O}_4$  compound.

The XPS etching response of E308-16 revealed an increase in Mn, Fe, Cr, and O suggesting that inner portions of particles are rich in metallic oxides. A large decrease in F intensity after etching suggests a fluoride-rich layer may coat many of the particles. Peak locations of Cr were not clearly discernible; however, they were located within the regime of  $\text{Cr}_2\text{O}_3$  ( $\text{Cr}^{+3}$ ),  $\text{CrO}_2$  ( $\text{Cr}^{+4}$ ), and  $\text{CrO}_3$  ( $\text{Cr}^{+6}$ ), which suggests a presence of  $\text{Cr}^{+6}$  in the fume, though this observation is unsubstantiated. To reveal this indisputably, other methods would be required such as wet chemical testing (Ref. 17). However, the compound  $\text{K}_2\text{CrO}_4$  ( $\text{Cr}^{+6}$ ) was observed in XRD results (Ref. 1), which agrees with the current XPS observations.

### Practical Implications

Fume characterization is relevant in understanding the impact of fume exposure on the health and safety of welding personnel. The data provided in studies, including this one, are important to consumable manufacturers, the industrial hygiene commu-

nity, and government bodies that sanction the regulations regarding exposure. It is apparent that fume must be collected and separated into sizes where the appropriate characterization technique may be applied to study fume particles in the different size ranges. In conjunction, it is also imperative that fume particle size and mass distributions are measured, because they provide insight into the physical phenomena governing formation of welding fume. Coupling advanced particle sizing techniques, such as use of the ELPI, with the advanced characterization techniques including HR-SEM, HR-TEM, and XPS, provides a more complete study. Though there is much to be gained from studying welding fume, a few benefits are as follows:

- Evaporative losses of elements during welding can result in changes in weld deposit composition. Also, vaporization of core wire and flux constituents controls fume generation rates. Therefore, core wire and flux compositions may be adjusted to compensate for this during consumable formulation.

- Particle size distribution measurements (number and mass) provide a gauge to the industrial hygiene community of potential interactions that particles will have with the body. Knowledge of fume composition and chemistry allows the hygiene community to determine what epidemiological effects may result upon interaction with human tissues.

- Government regulations concerning worker exposure to welding fumes should be continually updated as characterization techniques provide additional information regarding composition and chemistry. This is also true of new welding consumables as they come into widespread use.

### Conclusions

1. An electrical low pressure impactor (ELPI) was used to collect SMAW fume and separate the particles by aerodynamic diameter, allowing for the different size ranges to be imaged and analyzed with the appropriate analytical methods according to particle size.

2. Fume particles generated by the SMAW process vary across a large size range (several nm to several  $\mu\text{m}$ ), which requires the use of multiple imaging and chemical analysis techniques to fully characterize the fume.

3. The SEM, TEM, and HR-TEM were used to characterize both individual particles as well as the bulk fume on each ELPI stage for three SMAW electrode fumes. This revealed three unique particle structures: spherical, irregular, and agglomerate.

4. The SEM was used to image fume particles and examine the morphology of particles greater than 0.3  $\mu\text{m}$ . The largest per-

cent of particles on all stages of the ELPI were agglomerates of spherical particles. Individual spherical particles were common to all fumes, but were found in lesser frequency than the agglomerates. Agglomeration was common because metal aerosols are typically highly charged or may sinter at high temperature, providing different mechanisms for particles to adhere together. Irregular-shaped particles were also found in fumes from each electrode, but were not as common as agglomerations or individual spherical particles.

5. The TEM and HR-TEM were used to image nano-scale particles. Most of the ultrafine particles had a crystalline structure, and some particles exhibited a core-shell structure.

6. Chemical analysis techniques used during this investigation included SEM-XEDS, TEM-XEDS, and XPS. The XEDS as a fume analysis technique is limited by the size of the electron beam and interaction volume with the particle, and its inability to accurately analyze light elements. Therefore, SEM-XEDS was limited to analysis of particles above 0.3  $\mu\text{m}$ , and TEM-XEDS was used for particles below this size range.

7. Compositional variations were observed with SEM-XEDS across the collected particle size range, and individual particle analyses generally were within bulk compositions on each stage. TEM-XEDS and SAD showed that ultrafine particles were typically metal oxides of the form  $(\text{M,Fe})_3\text{O}_4$ , where M may be substituted for Mn and Cr, though different compounds were found when particles exhibited a core-shell microstructure.

8. The XPS confirmed the core-shell morphology by partial depth profiling and revealed that the most likely valence states for Fe and Mn are +2 and +3, because they are found largely in the  $(\text{M,Fe})_3\text{O}_4$  compound. Examination of E308-16 fume revealed valence states corresponding to  $\text{Cr}^{+6}$  bearing compounds, which agrees with XRD results in Part 1.

### Acknowledgments

The authors would like to thank Matt Gonsler of the Welding & Joining Metallurgy Group at The Ohio State University for his valuable assistance in fume collection and analysis. Also, thanks to Troy Paskell of WeldQC for help with equipment setup and testing. Funding for this project was provided by D&L Welding Fume Analysis LLC representing a consortium of past and current consumable manufacturers.

### References

1. Sowards, J. W., Lippold, J. C., Dickinson, D. W., and Ramirez, A. J. 2008. Characterization of welding fume from SMAW electrodes —

Part I. *Welding Journal* 87(4): 106-s to 112-s.

2. Marjamaki, M., Keskinen, J., Chen, D.-R., and Pui, D. Y. H. 2000. Performance evaluation of the electrical low pressure impactor (ELPI). *Journal of Aerosol Science* 31(2): 249-261.

3. Jenkins, N. T., and Eager, T. W. 2005. Chemical analysis of welding fume particles. *Welding Journal* 84(6): 87-s to 93-s.

4. Spurny, K. R., ed. 1999. *Analytical Chemistry of Aerosols*. Boca Raton, Fla.: Lewis Publishing.

5. Sowards, J. W., Ramirez, A. J., Lippold, J. C., and Dickinson, D. W. 2008. Characterization procedure for analysis of arc welding fume. *Welding Journal* 87(3): 76-s to 83-s.

6. Smith, G. C. 1994. *Surface Analysis by Electron Spectroscopy*. New York: Plenum Press.

7. Voitkevich, V. G. 1988. Investigation of heterogeneity of welding fume particle composition by the method of X-ray photoelectron

spectroscopy. *Welding in the World* 26(5-6): 108-111.

8. Tandon, R. K., Payling, R., Chenhall, B. E., Crisp, P. T., Ellis, J., and Baker, R. S. 1985. Application of X-ray photoelectron spectroscopy to the analysis of stainless-steel welding aerosols. *Applications of Surface Science* 20(4): 527-537.

9. Zimmer, A. T. 2002. The influence of metallurgy on the formation of welding aerosols. *Journal of Environmental Monitoring* 4: 628-632.

10. Jenkins, N. T. 2003. Chemistry of airborne particles in metallurgical processing. PhD dissertation, Massachusetts Institute of Technology.

11. Zimmer, A. T., and Biswas, P. 2001. Characterization of the aerosols resulting from arc welding processes. *Journal of Aerosol Science* 32(8): 933-1008.

12. Konarski, P., Iwanek, I., and Cwil, M. 2003. Core-shell morphology of welding fume micro- and nanoparticles. *Vacuum* 70: 385-389.

13. Maynard, A. D., Ito, Y., Arslan, I., Zimmer, A. T., Browning, N., and Nicholls, A. 2004. Examining elemental surface enrichment in ultrafine aerosol particles using scanning transmission electron microscopy. *Aerosol Science and Technology* 38: 365-381.

14. Sowards, J. W. 2006. Characterization of aerosol generated by arc welding processes. MS thesis, The Ohio State University.

15. Kobayashi, M., Maki, S., Hashimoto, Y., and Suga, T. 1983. Investigations on chemical composition of welding fumes. *Welding Journal* 62(7): 190-s to 196-s.

16. Jenkins, N. T., and Eager, T. W. 2003. Submicron particle chemistry: vapor condensation analogous to liquid solidification. *JOM Journal of the Minerals, Metals and Materials Society* 55(6): 44-47.

17. Kimura, S., Kobayashi, M., Godai, T., and Minato, S. 1979. Investigation on chromium in stainless steel welding fumes. *Welding Journal* 58(7): 195-s to 204-s.

## Preparation of Manuscripts for Submission to the *Welding Journal* Research Supplement

All authors should address themselves to the following questions when writing papers for submission to the *Welding Research Supplement*:

- Why was the work done?
- What was done?
- What was found?
- What is the significance of your results?
- What are your most important conclusions?

With those questions in mind, most authors can logically organize their material along the following lines, using suitable headings and subheadings to divide the paper.

1) **Abstract.** A concise summary of the major elements of the presentation, not exceeding 200 words, to help the reader decide if the information is for him or her.

2) **Introduction.** A short statement giving relevant background, purpose, and scope to help orient the reader. Do not duplicate the abstract.

3) **Experimental Procedure, Materials, Equipment.**

4) **Results, Discussion.** The facts or data obtained and their evaluation.

5) **Conclusion.** An evaluation and interpretation of your results. Most often, this is what the readers remember.

### 6) **Acknowledgment, References and Appendix.**

Keep in mind that proper use of terms, abbreviations, and symbols are important considerations in processing a manuscript for publication. For welding terminology, the *Welding Journal* adheres to AWS A3.0:2001, *Standard Welding Terms and Definitions*.

Papers submitted for consideration in the *Welding Research Supplement* are required to undergo Peer Review before acceptance for publication. Submit an original and one copy (double-spaced, with 1-in. margins on 8 1/2 x 11-in. or A4 paper) of the manuscript. A manuscript submission form should accompany the manuscript.

Tables and figures should be separate from the manuscript copy and only high-quality figures will be published. Figures should be original line art or glossy photos. Special instructions are required if figures are submitted by electronic means. To receive complete instructions and the manuscript submission form, please contact the Peer Review Coordinator, Erin Adams, at (305) 443-9353, ext. 275; FAX 305-443-7404; or write to the American Welding Society, 550 NW LeJeune Rd., Miami, FL 33126.